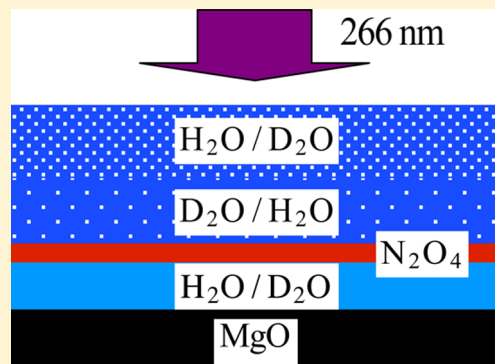


Amorphous Solid Water: Pulsed Heating of Buried N_2O_4 Jaimie Stomberg,[†] Stephanie McKean,[†] Christopher Larson,[†] H. Reisler,^{*} and C. Wittig^{*}

Department of Chemistry, University of Southern California, Los Angeles, California 90089, United States

S Supporting Information

ABSTRACT: Molecular transport and morphological change were examined in films of amorphous solid water (ASW). A buried N_2O_4 layer absorbs pulsed 266 nm radiation, creating heated fluid. Temperature and pressure gradients facilitate the formation of fissures through which fluid travels to (ultra)high vacuum. Film thickness up to 2400 monolayers was examined. In all cases, transport to vacuum could be achieved with a single pulse. Material that entered vacuum was detected using a time-of-flight mass spectrometer that recorded spectra every 10 μs . An ASW layer insulated the N_2O_4 layer from the high-thermal-conductivity MgO substrate; this was verified experimentally and with heat-transfer calculations. Laser-heated fluid strips water from fissure walls throughout its trip to vacuum. Experiments with alternate H_2O and D_2O layers reveal efficient isotope scrambling, consistent with water reaching vacuum via this mechanism. It is likely that ejected water undergoes collisions just above the film surface due to the high density of material that reaches the surface via fissures, as evidenced by complex temporal profiles extending past 1 ms. Little material enters vacuum after cessation of the 10 ns pulse because cold ASW near the film surface freezes material that is no longer being heated. A proposed model is in accord with the data.



1. INTRODUCTION

Molecular transport and morphological change were examined in a form of low-temperature solid water referred to as amorphous solid water (ASW). This material accounts for most of the water in the universe.¹ It has been the subject of intense research, motivated mainly by intellectual curiosity and the role it plays as a molecular factory in the interstellar medium (ISM).²

The Cassini spacecraft has orbited Saturn since 2004, and features of Saturn's moons have been revealed, including a subsurface water ocean and cryovolcanic activity on Enceladus.³ Water jets emanating from fissures in the solid water mantle extend hundreds of kilometers above the moon's surface,^{4,5} and its atmosphere contains CO_2 , H_2 , NH_3 , HCN , CH_2O , CO , CH_4 , and other light hydrocarbons. Enceladus is a candidate for hosting microbial life.⁵ Connections between the present work and related phenomena on Enceladus will be the subject of a future publication.

Molecular volcanoes in ASW have been examined thoroughly by Kay and co-workers.^{6,7} These are eruptions in which buried material is heated by a temperature ramp ($\sim 1 \text{ K s}^{-1}$), resulting in its explosive release at the temperature where the ASW turns into crystalline ice. Likewise, we have used infrared radiation to initiate vigorous release of water monomer and small clusters.⁸ The goal of the present study is to reveal and understand phenomena that take place when heat is implanted in buried strata. Pursuant to this, processes that involve films doped with an N_2O_4 layer (Figure 1) are reported. The N_2O_4 layer serves as a means of introducing heat.

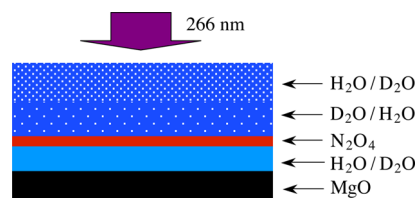


Figure 1. Schematic drawing indicating the structure of the films used in the present study. The black layer is the MgO substrate. Solid blue is an ASW layer that insulates the (red) N_2O_4 layer from the MgO, which has high thermal conductivity. The upper ASW layer can be H_2O , D_2O , or a combination. Samples are prepared and studied under UHV conditions.

Films are prepared by vapor deposition at around 100 K. Properties of vapor-deposited ASW depend on temperature, rate, method, and substrate, so conditions need to be specified.⁹ In the range 130–155 K, what existed as ASW at lower temperatures is a highly viscous liquid.^{1,10} It converts to cubic ice at 155 K and hexagonal ice at higher temperatures.¹¹

Photolysis (10 ns, 266 nm) of the N_2O_4 layer creates heated fluid. Temperature and pressure gradients facilitate the formation of fissures through which nitrogen oxides and water travel to vacuum. The N_2O_4 layer and the N_2O_4 -rich fluid that passes through fissures are heated by the 10 ns pulse, and

Special Issue: Steven J. Sibener Festschrift

Received: October 29, 2014

Revised: April 22, 2015

Published: April 23, 2015



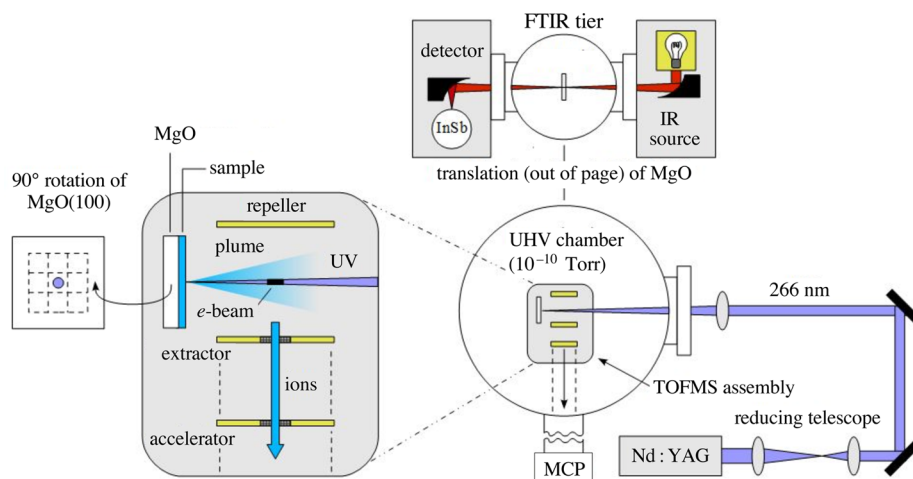


Figure 2. UHV chamber equipped with TOFMS and FTIR diagnostics. Radiation (266 nm) excites the sample at normal incidence, causing material to enter the gas phase. The black rectangle labeled *e*-beam indicates the portion of the ionized region that is extracted through the mesh aperture that lies below it in the figure. Ions are extracted at a repetition rate of 100 kHz. Samples deposited on the MgO(100) surface can be irradiated in nine areas, indicated on the left, to achieve signal averaging while maintaining single-pulse conditions. For the FTIR studies, the focusing lens is removed and an approximately 3 mm diameter area is irradiated. The surface is then translated to the upper tier. IR radiation is brought to a focus at the surface using a parabolic mirror. It is then focused onto the InSb detector using a second parabolic mirror.

heated fluid traveling through fissures strips water from the walls.

The experimental strategy and details are presented in section 2. Representative data are presented in section 3, with additional data given as Supporting Information. In section 4, the results are discussed and a model is proposed.

2. EXPERIMENTS

Experiments were conducted under ultrahigh (UHV) conditions (3×10^{-10} Torr) using pulsed (10 ns; 1–2 mJ) 266 nm radiation and a high repetition rate time-of-flight mass spectrometer (TOFMS; Jordan TOF Products). An upper tier accommodates temperature programmed desorption (TPD) and Fourier transform infrared (FTIR) spectroscopy. A lower tier is configured for TOFMS measurements (Figure 2).^{12–14}

The MgO substrate was prepared by cleaving a crystal (MTI Corporation) on each side in dry N_2 . The $0.8 \times 10 \times 10$ mm³ substrate was then transferred to the UHV chamber. Oxygen vacancies were filled through exposure to 10^{-7} Torr of O_2 while annealing at 600 K for an hour. This procedure has been shown to produce a high-quality MgO(100) surface.^{12–15}

The substrate was clamped in 0.3 mm thick copper foil (ESPI Metals). A 6×6 mm² aperture in the foil enabled radiation to pass through. It was then attached to the arm of one of two electrically isolated copper blocks mounted on a copper-capped stainless steel coldfinger on a LN_2 reservoir (Kurt Lesker, altered by McAllister Technical Services). This configuration enabled the surface to be cooled to 100 K. Temperature was monitored using a K-type thermocouple bonded (Ceramabond 835-M, Aremco Products) bonded to one side of the MgO surface. A tantalum wire cemented to the back of the copper housing of the surface was used for resistive heating. The cryostat was fitted with bellows, and the sample holder was capable of XYZ translation and 360° rotation.

Samples were grown at 100 K. Layers were deposited after heating to ~ 200 K to remove condensed background gas, and then cooling it to 100 K. All gases except NO_2 were deposited using background dosing. Because NO_2 reacts with metal

surfaces, a 0.75 cm ID \times 23 cm glass tube was fixed to a precision leak valve for a degree of directed dosing. The surface was rotated from the TOF position such that the end of the tube was ≈ 4 cm from the surface, with the tube oriented normal to the surface. Following deposition, the surface was rotated back to the TOF position.

Water layer thickness is reported in monolayers (ML). Under our deposition conditions, 1 Langmuir (10^{-6} Torr-seconds) of H_2O formed 1.67 ML on the MgO surface at 100 K. This has been verified previously by comparing the integrated intensities of the monolayer peak to the multilayer peak using TPD.¹² Similar sticking probabilities are expected for NO_2 . However, we do not have experimental verification of NO_2 deposition rate, so those layers are reported in Langmuirs (L).

Deposition of NO_2 takes place through a combination of directed and background dosing. The glass tube carrying NO_2 is aimed at the surface and also creates background NO_2 . Experiments were carried out to assess this dosing arrangement. Water was used rather than NO_2 because it was easy to measure the amount of deposited material using FTIR, as discussed later in this Section and demonstrated (vide infra) in section 3.6. In these experiments, H_2O was deposited at 102 K: first by background dosing, then with directed dosing at the same background partial pressure as with background dosing alone (2×10^{-7} Torr for 5 min = 60 L).

FTIR spectra were recorded in each case (Figure 3). H_2O and NO_2 have sticking coefficients near 1 at this temperature. To account for the fact that background H_2O deposits on each side of the substrate, the area of the background-dosing signal was divided by two and subtracted from the areas of the background and direct dosing signals. Directed dosing increased front-surface deposition by about 70% over background dosing alone.

The 266 nm radiation was the fourth harmonic of a Nd:YAG laser (Continuum PL9010, 10 Hz). A chopper wheel (ThorLabs MC1000) was used to select every tenth pulse. Beam diameter was reduced from 8 mm to 3 mm using a

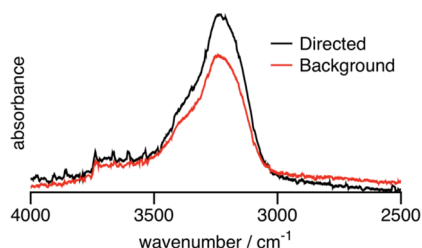


Figure 3. FTIR spectra. Directed dosing increases front-surface deposition.

telescope. This radiation was focused to ~ 0.3 mm diameter at the substrate using a 50 cm focal length CaF_2 lens.

The TOFMS was a Wiley–McLaren design with three electrode plates and an electron beam source 25 mm from the surface. Triggering at 100 kHz yielded a mass spectrum every 10 μs . Laser irradiation resulted in material passing through the ionizing region (Figure 2). The plume was subjected to 70 eV electron ionization. The plates were held at 1800 V, and positive ions were extracted every 10 μs by dropping the potential on the extractor plate to 1550 V for 3 μs . Ions were then accelerated using a grounded third plate, after which they entered the 48 cm field-free drift tube. They were detected at the end of the drift tube using a multichannel plate (MCP) detector connected to a fast preamplifier (SRS D-300 MHz). The amplified current from the MCP was recorded on a computer with an analog-to-digital converter (Gage CS 8500, 8 bit, 512k samples). Spectra were collected using a custom LabView program (National Instruments) and further processed using IGOR Pro (WaveMetrics). The set of 30–120 individual mass spectra collected following a single laser pulse shall be referred to hereafter as a “temporal profile”.

The arrival time of a species at a small volume in the ionization region can reflect its speed when $v = d/t$ applies, where d is the distance the species travels prior to its ionization and the species departs from the surface at $t = 0$. The size and shape (12 mm diameter) of the extraction region limits resolution. Species having a given speed and departing from the surface at $t = 0$ in general might arrive at different parts of the extraction region. Consequently, a given speed contributes to the signal at different times. Likewise, different speeds contribute to the signal at a given extraction time. We accepted low velocity resolution in the present experiments as a tradeoff in favor of large signal-to-noise ratio (S/N), which enabled us to obtain high-quality spectra following a single laser pulse.

Nine spots in a 3×3 grid could be irradiated per surface to give nine individual temporal profiles. This provided the option of averaging to improve S/N and reduce effects due to laser energy fluctuation and film irregularity. This averaging method is applied to whichever pulse we are interested in (first, second, etc.). Because of the limited horizontal diffusion of absorbed laser energy, moving the laser position by 1 mm ensured irradiation of an undisturbed section of the film.

FTIR spectra were collected using a Nicolet Protegé 460 spectrometer equipped with a LN_2 -cooled InSb detector. Spectra were recorded using OMNIC software. The range $1850\text{--}7000\text{ cm}^{-1}$ was covered at 1 cm^{-1} resolution, averaging 200 scans. The IR beam was trimmed using an iris to 2 mm diameter to ensure that it sampled the part of the surface that was irradiated. To collect an FTIR spectrum, the surface was raised to the top tier to collect a background. The surface was then lowered to the middle tier for the dosing procedure and

then raised again to collect a baseline FTIR spectrum. After the surface was lowered again, the 50 cm CaF_2 focusing lens was removed from the 266 nm beam path to give a roughly 3 mm diameter beam centered on the surface. Following 266 nm irradiation, the surface was raised again to take the final spectrum.

3. RESULTS

Time-of-flight mass spectra and temporal profiles were recorded for molecules that enter the gas phase following 266 nm irradiation using the sandwich arrangement indicated in Figure 1. To interpret these spectra, it was necessary to obtain individual spectra of the stable molecules that arise in the experiments: N_2O_4 , NO_2 , NO , and H_2O . It is noteworthy that N_2O_4 yields no ions more massive than NO_2^+ , which complicates distinguishing N_2O_4 from NO_2 . In addition, temporal profiles and their individual mass spectra were recorded for material released into vacuum following the 266 nm irradiation of exposed N_2O_4 . These data are presented in section 3.1.

In section 3.2, mass spectra and temporal profiles are presented for the first laser pulse to interact with freshly prepared samples, such as the one indicated in Figure 1. The TOFMS diagnostic provides excellent single-shot S/N. Results for the second, third, etc. pulses incident on the same spot are presented in section 3.3. As discussed in section 2, no signal averaging is carried out for TOFMS results from successive pulses that fall incident on the same spot. In other words, effects due to the first, second, third, etc. pulses are isolated from one another. In section 3.4, it is shown that material ejection takes place through fissures that originate at the laser-heated region. At low fluence, the progress of the N_2O_4 -rich material toward vacuum stops short of ejecting material. A second (or third) pulse acts on the trapped material in the incipient fissure, enabling it to enter vacuum. Experimental results obtained using layers of D_2O and H_2O in the upper ASW are presented in section 3.5, demonstrating that water that enters vacuum comes from the fissure walls. Preliminary results obtained using the FTIR probe are presented in section 3.6.

3.1. Mass Spectra of NO_2 , N_2O_4 , NO , and H_2O . Data analyses make use of comparisons between mass spectra, including subtracting contributions from species whose spectra are known with good accuracy. Therefore, mass spectra of NO_2 , N_2O_4 , NO , and H_2O were recorded using our apparatus, as opposed to relying on spectra taken from the literature. This obviates the need to account for differences due to experimental arrangements, e.g., time-of-flight versus quadrupole. Relevant mass spectra are shown in Figure 4. Those for NO_2 , NO , and H_2O can be found in the literature. Nonetheless, we find that our cracking patterns differ slightly from those reported in the NIST database.¹⁶ The mass spectrum of gaseous N_2O_4 was not available in the literature. Its acquisition was more challenging, as discussed below.

3.1.1. N_2O_4 . Mass spectra of gaseous N_2O_4 were recorded by maintaining solid N_2O_4 at temperatures such that its sublimation provided adequate density in the ionization region of the TOFMS. Temperatures around 155 K were used. Impurity NO was minimized through the use of freeze–pump–thaw cycles, with the addition of O_2 during the warm phase. Lack of light blue color in the condensed material indicated minimal N_2O_3 , which is known to be present when there is an NO impurity.¹⁷ Furthermore, neutral NO yields a signal at m/e

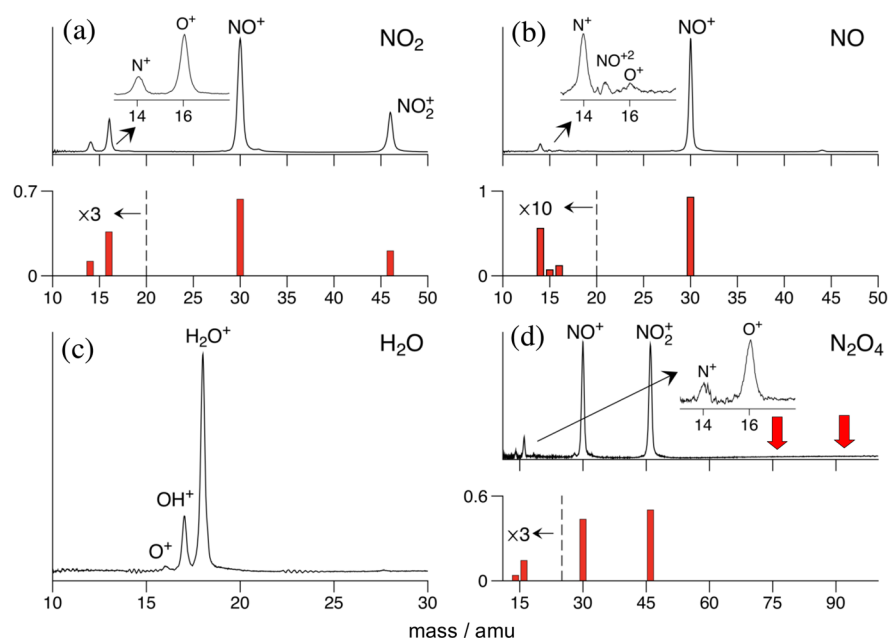


Figure 4. Mass spectra of NO_2 , NO , H_2O , and N_2O_4 . Ion percentages (areas of curves) are denoted by heights of red bars in the lower plots. (a) 300 K NO_2 gives $\text{NO}^+/\text{NO}_2^+ = 3.18$, $\text{O}^+/\text{NO}_2^+ = 0.58$, and $\text{N}^+/\text{NO}_2^+ = 0.19$. (b) 300 K NO gives $\text{O}^+/\text{NO}^+ = 0.01$ and $\text{N}^+/\text{NO}^+ = 0.06$; note the NO^{2+} signal at $m/e = 15$. (c) 300 K H_2O gives $\text{OH}^+/\text{H}_2\text{O}^+ = 0.27$, $\text{O}^+/\text{H}_2\text{O}^+ = 0.02$, and (not shown) $\text{H}^+/\text{H}_2\text{O}^+ = 0.07$. (d) The spectrum obtained using N_2O_4 sublimation at ~ 155 K gives $\text{NO}^+/\text{NO}_2^+ = 0.9$, $\text{O}^+/\text{NO}_2^+ = 0.1$, and $\text{N}^+/\text{NO}_2^+ = 0.02$. Note the absence of signal at 76 and 92 amu (N_2O_3^+ and N_2O_4^+ , red arrows).

$= 15$ due to NO^{2+} ,¹⁶ as seen in Figure 4. This is absent in spectra such as the one shown in Figure 4d. Finally, the dissociation $\text{N}_2\text{O}_4 \rightarrow 2\text{NO}_2$ is endoergic by 4440 cm^{-1} ,¹⁸ whereas the binding energy of an N_2O_4 molecule to its solid is 3800 cm^{-1} .¹⁹ For NO_2 to enter the gas phase during sublimation, it would be necessary to break the N–N bond in N_2O_4 and have NO_2 desorb. The difference between the energies required to enter the gas phase for N_2O_4 versus NO_2 augurs for a small percentage of NO_2 leaving the film. To the best of our knowledge, this is the first report of a direct measurement of the cracking pattern of this molecule.

Considering Figure 4d, 70 eV electron impact ionization of N_2O_4 yields no ions heavier than NO_2^+ , i.e., neither N_2O_4^+ nor N_2O_3^+ is observed. The red arrows indicate where signals would have appeared had N_2O_4^+ and N_2O_3^+ been present. The fact that only NO^+ , NO_2^+ , O^+ , O_2^+ , and N^+ are present in spectra recorded using sublimation from condensed N_2O_4 presents a challenge insofar as assigning neutral parentages of ion signals. The amount of NO^+ relative to NO_2^+ is denoted $\text{NO}^+/\text{NO}_2^+$, where NO^+ and NO_2^+ are the areas of the respective signals; likewise for O^+/NO_2^+ and N^+/NO_2^+ . Neutral species, e.g., $\text{NO}_2/\text{N}_2\text{O}_4$, are denoted similarly. These latter ratios take into account the 70 eV ionization cross sections for N_2O_4 , NO_2 , NO , and O (Table 1), as discussed in the Appendix.

Figure 4d shows that N_2O_4 yields $\text{NO}^+/\text{NO}_2^+ = 0.9$ and $\text{O}^+/\text{NO}_2^+ = 0.1$. For 300 K NO_2 (Figure 4a), the values are 3.1 and 0.6, respectively. The large difference in $\text{NO}^+/\text{NO}_2^+$ values for NO_2 and N_2O_4 facilitates analyses.

If subliming N_2O_4 strikes a 300 K metal surface, it might stick and dissociate, yielding surface-bound NO_2 . In turn, NO_2 might be released into vacuum. This would yield a spectrum contaminated by NO_2 . This was checked using different electrode configurations in the TOFMS extraction region. When a significant amount of metal was placed opposite the

Table 1. 70 eV Ionization Cross Sections (10^{-16} cm^2)^a

species	cross section	species	cross section
N_2O_4	7.34	NO_2	3.53
NO	2.81	O_2	2.41
N_2	2.51	H_2O	2.28
O	1.36		

^aValues are from the NIST database,¹⁶ except N_2O_4 , which was computed.²⁰

sample (Figure 5a), the $\text{NO}^+/\text{NO}_2^+$ ratio increased to approximately 1.0. This modest but repeatable increase indicates the presence of NO_2 brought about through collisions

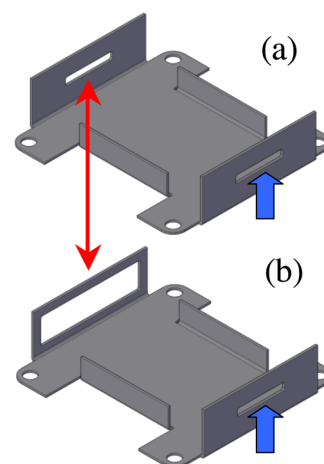


Figure 5. (a) Molecules passing through the lower right slot (blue arrow) into the ionization region encounter a large amount of metal on the other side. (b) Most of the metal on the other side has been removed (red arrow).

of N_2O_4 with the metal surface facing the plume. Without this added metal (Figure 5b), spectra such as the one in Figure 4d were recorded, giving an $\text{NO}^+/\text{NO}_2^+$ value of approximately 0.9 for N_2O_4 subliming at ≈ 155 K. There may be a modest amount of NO_2 contaminant, but the dominant N_2O_4 features are those shown in Figure 4d.

3.1.2. N_2O_4 atop H_2O . Next, 300 ML of H_2O covered by 80 L of N_2O_4 was irradiated with a 1 mJ, 266 nm pulse, yielding a broad temporal profile and individual mass spectra. Figure 6

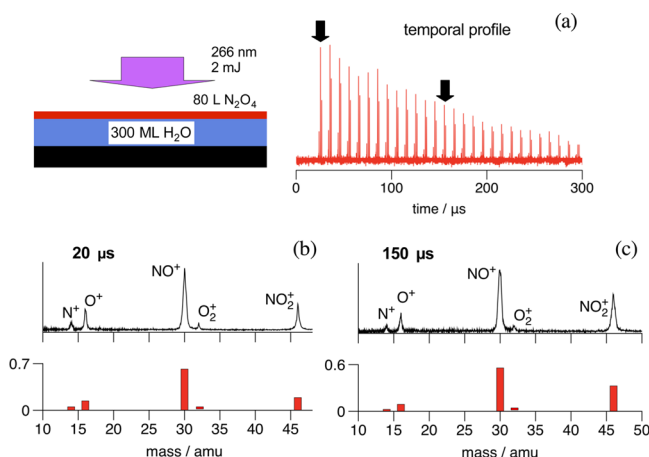


Figure 6. Extractions from the temporal profile at 20 and 150 μs (black arrows in panel a) yielding the mass spectra shown in panels b and c, respectively. The sample is depicted in the upper left; note the use of ML for H_2O and L for N_2O_4 . At 20 μs , NO_2 plays a significant role; its role is diminished at later times.

shows a typical single-shot (9-point average) result that characterizes exposed N_2O_4 . The variation of the $\text{NO}^+/\text{NO}_2^+$ ratio across the temporal profile depends on N_2O_4 and H_2O spacer layer thicknesses, whereas the overall profile shape is independent of these details. In the present study, the shape of the temporal profile serves as an indicator of exposed, as opposed to buried, N_2O_4 . Considering the upper left of Figure 6, 300 ML of H_2O provides thermal insulation against the high thermal conductivity of MgO ($250 \text{ W m}^{-1} \text{ K}^{-1}$ versus $\sim 1 \text{ W m}^{-1} \text{ K}^{-1}$ for ASW).^{21,22} Using D_2O in this layer, we have verified (FTIR and TOFMS) that there is no transport of water across the N_2O_4 layer. Figure 7 illustrates the role of the water spacer between MgO and N_2O_4 insofar as increasing signal intensity.

The first reliable mass spectrum in the temporal profile shown in Figure 6a is obtained for the 20 μs extraction, which corresponds to a speed of $\sim 1.2 \times 10^5$ cm/s. Arrival times yield crude estimates of speed because the transit time across the large ionization region is significant. In addition, the 3 μs extraction pulse that commences 20 μs after the laser firing

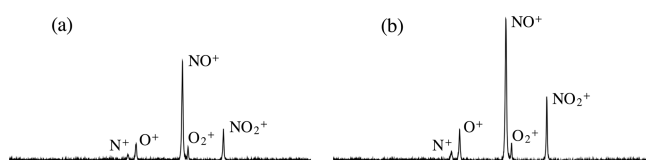


Figure 7. Mass spectra of exposed N_2O_4 subjected to focused 266 nm radiation (1 mJ): (a) no spacer between 80 L of N_2O_4 and MgO; (b) spacer of 300 ML of H_2O (Figure 6, upper left). Thermal insulation increased signal intensity.

follows a 7 μs duration ionization pulse, and these durations need to be taken into account. Notwithstanding these caveats, such estimates provide insight.

The kinetic energy of an NO_2 molecule whose speed is 1.2×10^5 cm/s is 2800 cm^{-1} . On the other hand, the speed of a species that leaves the surface at $t = 0$ and arrives at a point 2.5 cm from the surface 300 μs later (the last extraction in the temporal profile) is 8×10^3 cm/s. Were NO_2 and N_2O_4 to leave the surface at $t = 0$, the 300 μs arrival time would correspond to kinetic energies of 12.5 and 25 cm^{-1} , respectively. Later we will see that NO_2 most likely arises from photodissociation of gaseous N_2O_4 . The low energy of 25 cm^{-1} can be rationalized as being in the tail of a warm distribution. For example, the amount of signal in the 300 μs extraction is of order 1% of the total signal for the interval 0–300 μs .

The $\text{NO}_2/\text{N}_2\text{O}_4$ ratio can be expressed in terms of the respective numbers of ions: NO_2^+ , NO^+ , O^+ , and N^+ , as well as the N_2O_4 and NO_2 ionization cross-sections at 70 eV. An equation is derived in the Appendix that makes use of these quantities. It is given below:

$$\frac{\text{NO}_2}{\text{N}_2\text{O}_4} = 2.08 \frac{(\text{NO}^+/\text{NO}_2^+)F_{\text{N}_2\text{O}_4}^{\text{NO}_2^+} - F_{\text{N}_2\text{O}_4}^{\text{NO}^+}}{F_{\text{NO}_2}^{\text{NO}^+} - (\text{NO}^+/\text{NO}_2^+)F_{\text{NO}_2}^{\text{NO}_2^+}} \quad (1)$$

where $F_{\text{Y}}^{\text{X}^+}$ is the percentage of ion X^+ that derives from parent ion Y^+ . The number 2.08 is the ratio of the ionization cross sections for N_2O_4 and NO_2 (Table 1).

The data in Figure 4a,d were used to obtain values for the four F -factors in eq 1. Values of $\text{NO}^+/\text{NO}_2^+$ vary slightly at late times from one extraction to the next. Their average value is 0.95. When these numbers are used with eq 1, it is found that late times in the temporal profiles are dominated by N_2O_4 . The $\text{NO}_2/\text{N}_2\text{O}_4$ ratios obtained using eq 1 fluctuate around 0.2. This result is robust from one profile to the next, including extraction times later than the longest times in Figure 6a. This trend is also evident from visual inspection of the temporal profiles.

3.2. Single-Pulse Results. Samples such as those in Figure 1 are composed of a lower layer of H_2O or D_2O , an N_2O_4 layer (typically 80 L), and a range of ASW (H_2O and D_2O , either separately or in adjacent layers) upper layer thickness. Deposition is carried out near 100 K. It is possible that reaction takes place at interfaces between N_2O_4 and ASW yielding, for example, HNO_2 and HNO_3 .^{23,24} The extent of such reaction is not known. In addition, the porous nature of ASW accommodates penetration. These caveats notwithstanding, N_2O_4 is contained in a reasonably well-defined layer.

Figure 8 shows typical temporal profiles and individual spectra. Unless otherwise stated, ~ 1 mJ pulses were used. Rows 1, 2, and 3 correspond to ASW (H_2O) upper layers of 600, 1200, and 2400 ML, respectively; the ordinate scales are the same. The profile in row 1 shows that H_2O monomer arrives at the ionization region in two groups. On the other hand, NO_2^+ and NO^+ have profiles that differ from that of H_2O . The NO_2^+ peak arises from NO_2 and N_2O_4 , whereas the NO^+ peak arises from NO , NO_2 , and N_2O_4 . The NO contribution is modest, most likely arising from NO_2 photolysis. Hereafter, we shall refer to the combination of NO , NO_2 , and N_2O_4 as N_xO_y , and we shall refer to the $\text{NO}^+/\text{NO}_2^+$ ratio as R_N . The lumpy features in the water temporal profiles vary from one first-shot profile to the next. What is robust, however, is that lumpy

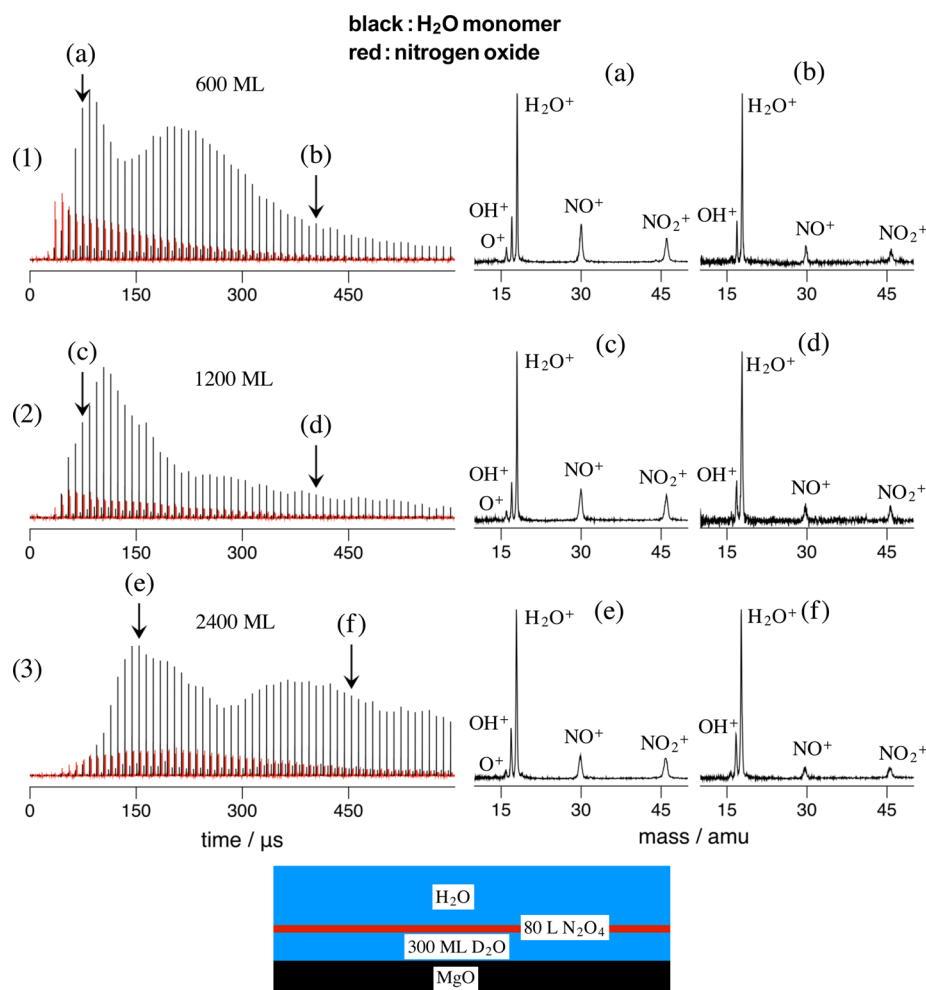


Figure 8. Temporal profiles and mass spectra for upper H_2O layer thickness: (1) 600 ML, (2) 1200 ML, and (3) 2400 ML. Each profile is the average of nine individual first-pulse profiles (1 mJ, 266 nm). Red corresponds to NO^+ and NO_2^+ . Black corresponds to H_2O^+ , OH^+ , and H^+ . The temporal profiles in rows 1–3 are on the same ordinate scale. The lower ASW layer is 300 ML of D_2O , and the N_2O_4 layer is 80 L. Mass spectra are shown in each row for the respective extractions in the temporal profiles indicated with vertical arrows. Sample composition is shown at the bottom.

Table 2. Peak Areas and R_N Values for the Spectra in Figures 8 and 11

pulse 1 (Figure 8)	amu			R_N	pulse 2 (Figure 11)	amu			R_N
	18	30	46			18	30	46	
a	1.92	1.27	0.95	1.34	a	0.18	5.35	1.97	2.72
b	1.86	0.40	0.40	1.00	b	2.12	1.18	0.72	1.64
c	1.86	1.14	1.01	1.13	c	0.42	5.30	1.70	3.12
d	2.82	0.49	0.44	1.11	d	2.39	2.46	1.38	1.78
e	2.64	0.89	0.95	0.94	e	0.00	5.51	1.80	3.06
f	2.75	0.38	0.45	0.84	f	3.45	1.14	0.91	1.25

features are always present, as seen also (vide infra) in Figure 10 and the Supporting Information.

The values of R_N for the Figure 8 spectra differ from one another, but none is close to the NO_2 value of 3.1 (Figure 4a). The largest is for row 1, spectrum a, which has $R_N = 1.34$ (Table 2). Many spectra have been examined, both within the profiles used in Figure 8 and in numerous other first-pulse profiles recorded over roughly a year. R_N is close to unity in essentially all of them, except at the shortest extraction times. Figure 9 shows R_N values for each extraction in the Figure 8 profiles.

Considering Figure 4d, the R_N value of 0.9 for N_2O_4 is close to the first-pulse ratios of Figure 8 (see Figure 9), except for the

first two extractions, which have low S/N. This differs markedly from the NO_2 value of 3.1. We conclude that N_2O_4 is the dominant N_xO_y constituent under the conditions of Figure 8. Row 2 of Figure 8 shows data for an upper ASW layer of 1200 ML. In light of the factor of 2 increase in upper ASW thickness, the amount of H_2O does not differ much from that of row 1. The upper ASW thickness for row 3 is four times that of row 1, and a propensity toward longer times is evident. The amount of H_2O that arrives at the ionization region is actually larger than that for rows 1 or 2. One might have expected additional thickness to inhibit material from entering vacuum, e.g., because of increased heat capacity.

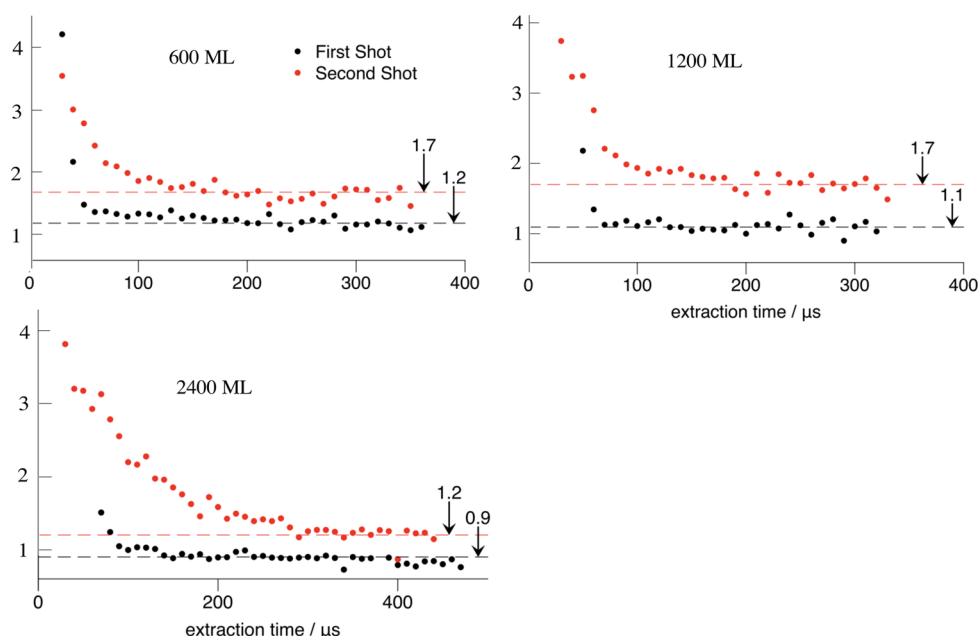


Figure 9. R_N values for a large number of extractions. First-pulse R_N values (black) settle down after the first few extractions to values of order unity. Second-pulse R_N values (red) are consistent with the presence of a significant amount of N_2O_4 in the surface region.

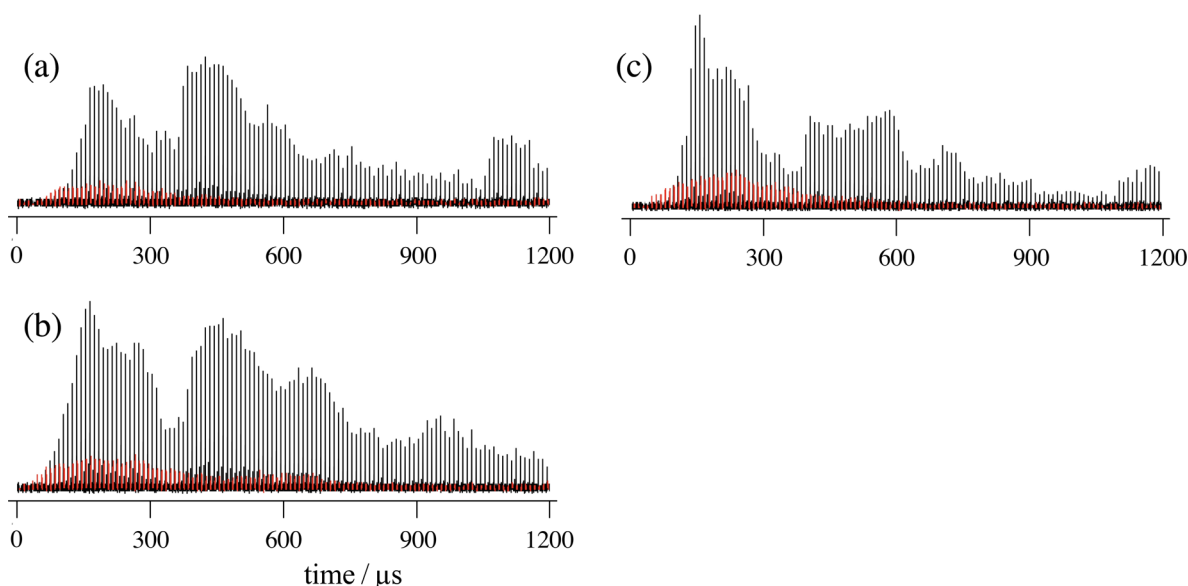


Figure 10. Temporal profiles of desorbed material for different spots on 2400 ML of ASW. Each panel is a single, first-pulse temporal profile. Red corresponds to NO^+ and NO_2^+ , black to H_2O . See Supporting Information for additional data.

3.2.1. Temporal Profiles. There is no possibility that the majority of the H_2O detected mass spectrometrically leaves the film at $t = 0$ and travels without collision to the ionization region. For example, a transit time τ of 200 μs and $v = d/\tau$, with $d = 2.5$ cm, yields kinetic energy of 10 cm^{-1} . H_2O signal beyond 200 μs would correspond to kinetic energies <10 cm^{-1} . Figure 10 shows significant signal out to 1200 μs , which corresponds to kinetic energy of 0.3 cm^{-1} . In section 4 it is shown that the upper ASW is too thick to accommodate sublimation; H_2O that enters vacuum does so via fissures. The lumpy character is in accord with molecules undergoing collisions as they emerge from the fissures.

3.3. Subsequent Pulses Incident on the Same Spot. The first pulse to interact with a sample alters it significantly.

Thus, we studied effects brought about by subsequent pulses, albeit one at a time. Figure 11 shows profiles and spectra for second pulses incident on the same spots as were the first. Results from all nine spots are summed. A striking effect is seen in the N_xO_y profiles. The R_N values obtained for each of them (Table 2 and Figure 9) resemble those of exposed N_2O_4 (Figure 6). This supports a model in which robust fissures are formed with the first pulse, through which N_xO_y can be transported to the surface region with subsequent pulses. The R_N values for the earliest extractions in each profile indicate that NO_2 photoproduct reaches the mass spectrometer, confirming that N_2O_4 is already present at the surface. In light of the role played by 266 nm photodissociation of N_2O_4 , it is not feasible

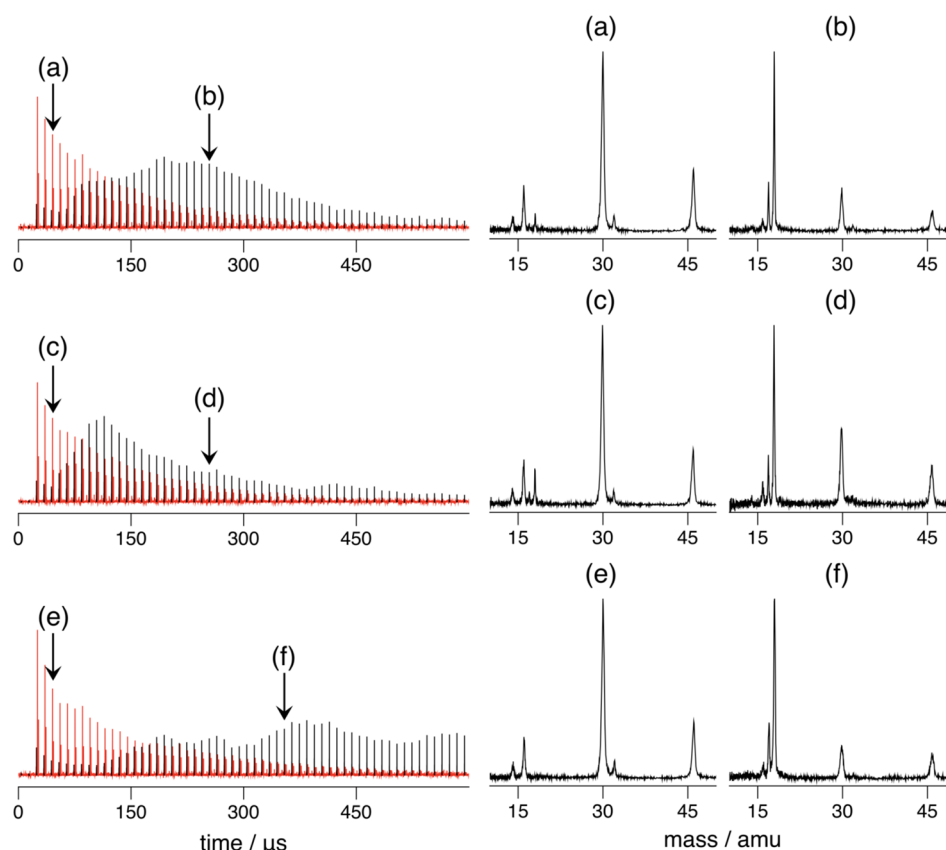


Figure 11. Temporal profiles for a second 1 mJ laser pulse at the same locations as in Figure 8. Each profile is the sum of profiles from nine spots. Red corresponds to NO^+ and NO_2^+ , black to H_2O . The ordinate scale is the same as in Figure 8. Mass spectra are shown on the right for the respective extractions in the temporal profiles indicated with vertical arrows on the left.

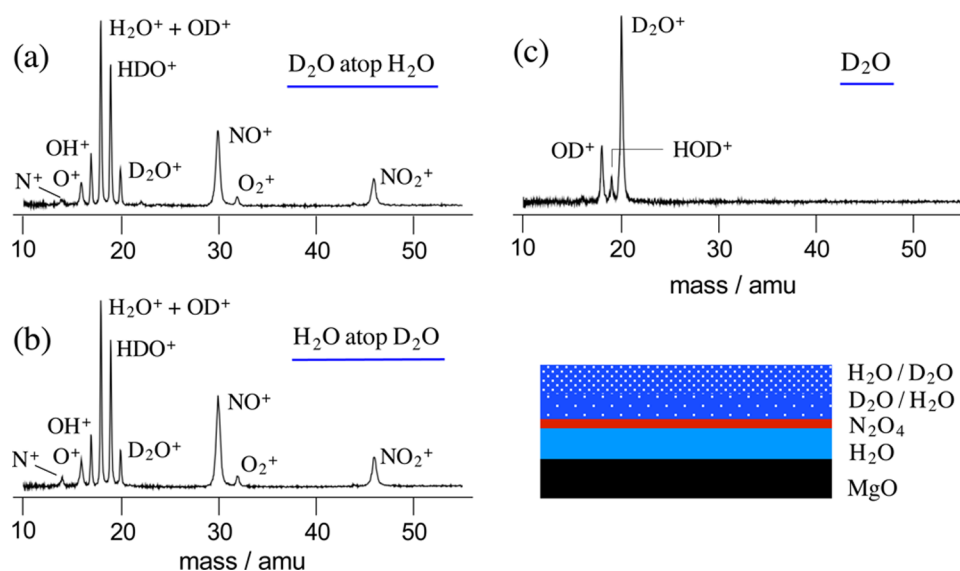


Figure 12. (a,b) Spectra for extractions at 50–60 μs , following first-pulse 266 nm irradiation (1.5 mJ) for samples that have 80 L of N_2O_4 atop a 300 ML H_2O spacer and alternating H_2O and D_2O upper layers. In panel a, the upper ASW layer has 200 ML of D_2O atop 200 ML of H_2O , and in panel b this is reversed. In panel c, a spectrum of 300 K gaseous D_2O recorded the same day shows only modest HDO contamination.

to determine quantitatively the respective amounts of gas-phase N_2O_4 and NO_2 .

3.4. Fissure Growth in Stages. The results presented in sections 3.2 and 3.3 indicate the formation of fissures through which material passes on its way to vacuum. This process depends on laser fluence. With fluence lowered by an order of

magnitude (at constant energy), the first pulse yielded no signal, whereas a second (or sometimes third) pulse yielded signal. Subsequent pulses yielded significant signal, and the N_xO_y temporal profiles displayed the characteristic shape and mass spectra of exposed N_2O_4 , as in Figure 6. Apparently the first pulse pushes fluid toward vacuum, but with insufficient

thrust for it to exit the film. Competition between moving toward vacuum versus depositing on fissure walls favors the latter to the extent that nothing exits the film.

The next pulse heats the N_2O_4 reservoir plus the N_2O_4 -rich material trapped in incipient fissures, resulting in material entering vacuum. Sometimes a third pulse is required. This behavior is in accord with the model discussed in section 4.

3.5. Isotope Scrambling: Scraping the Walls. H/D isotope exchange (scrambling) sheds light on the mechanism of material transport. Figure 12 shows an example of facile H/D exchange that takes place when layers of D_2O and H_2O are placed atop N_2O_4 and the sample is irradiated. The samples were prepared at 100 K, at which temperature there is no exchange.²⁵ This was verified using FTIR.

The mass spectra shown in Figure 12a,b indicate that extensive exchange has occurred during the heated fluid's transit through the fissures. The upper ASW is composed of 200 ML each of D_2O and H_2O : (a) D_2O over H_2O and (b) H_2O over D_2O . This corresponds to an upper ASW thickness of roughly 140 nm, and exchange can occur only in the top half. This facile exchange underscores the heated nature of the fluid passing through the fissures and efficient mixing of H_2O and D_2O . The extent to which traces in Figure 12a,b resemble one another is striking. These data indicate that water is removed by the heated fluid from the fissure walls throughout the length of the fissure. The trace in Figure 12c is a check. It shows that there is little isotope scrambling due to impurity H_2O when 300 K gaseous D_2O is introduced into the chamber.

3.6. FTIR. It is desirable to record the production and removal of species under single-pulse conditions by using FTIR. This has not yet been achieved because of insufficient fluence and the limited spectral range of the InSb detector. However, we have recorded FTIR spectra that demonstrate water removal from the upper ASW. As mentioned earlier, the (D_2O) spacer between MgO and N_2O_4 is robust. Not once has it crossed the N_2O_4 layer.

Considering Figure 13, 14% of the upper ASW layer has been removed by irradiation with 70 pulses. The fluence is at least an

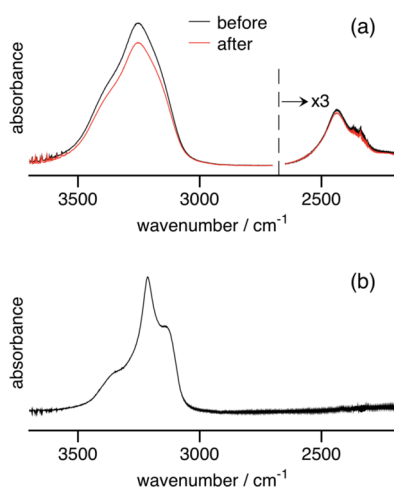


Figure 13. (a) FTIR spectra using 300 ML D_2O , 80 L N_2O_4 , and 2400 ML H_2O , deposited at 100 K and irradiated with 70 pulses (6 mJ, 3 mm diameter spot). The OD peak at $\approx 2400\text{ cm}^{-1}$ is unchanged, whereas the OH peak has decreased by 14%. (b) 2400 ML of H_2O has been annealed at 165 K for 10 min to induce crystallization. The “after” spectrum in panel a does not appear more crystalline after irradiation.

order of magnitude lower than that used in the TOFMS studies. The amorphous nature of the water is unchanged, as evidenced by the spectra in Figure 13a,b.

4. DISCUSSION

The data, together with a few straightforward estimates, led us to propose a model for material transport from the N_2O_4 layer to vacuum via fissures. Before starting the experiments, we expected that an ASW upper layer of several tens of ML would result in a modest amount of material entering the gas phase and that several hundred ML would result in virtually nothing entering the gas phase. In fact, the thickest ASW layer used, 2400 ML, yielded the largest amount of released material.

4.1. Observables. Before discussing the model, it is useful to summarize the experimental observations. First, the transport of material to vacuum via pulsed heating of buried layers differs qualitatively from that of pulsed heating of samples of uniform composition. For example, small protonated water clusters have not been observed in any of the mass spectra recorded in the present study, whereas they are readily observed when exciting ASW/ CO_2 mixtures using focused infrared radiation in the OH-stretch region.⁸ This underscores the fact that the mechanisms for the transport of material to vacuum differ for these two cases. Second, the phenomena described here and the so-called “volcano peak”, where embedded atoms and molecules are ejected from ASW upon heating,¹¹ are different. The latter involves homogeneous thermal heating of the film and the abrupt expulsion of guest molecules at a temperature corresponding to the phase transition to cubic ice. Our experiments involve selective pulsed heating of an embedded layer covered by a relatively thick ASW layer, followed by transport of the heated fluid to vacuum.

The 266 nm photolysis of gaseous N_2O_4 yields NO_2 with translational and internal energy. In the dense environments of the present experiments, recombination takes place, and nascent excitations evolve to heat on a time scale that is much shorter than the pulse duration. The net effect is heating the N_2O_4 layer and its surroundings.

Molecules detected by TOFMS include N_2O_4 , NO_2 , NO , H_2O , and O_2 . When the upper ASW is composed of H_2O and D_2O layers, HDO and D_2O are also detected. The amount of NO is modest, and it shall not be considered further. Using D_2O to insulate N_2O_4 from the MgO substrate distinguishes this layer spectrally from H_2O atop the N_2O_4 . Molecules in the insulator layer never pass through the N_2O_4 .

Temporal profiles and mass spectra obtained with ASW-covered versus exposed N_2O_4 are revealing. For the former, the first pulse liberates mainly N_2O_4 . This manifests as an R_N value much smaller than that for NO_2 (0.9 versus 3.1). On the other hand, a signature of exposed N_2O_4 is the presence of gas-phase NO_2 photoproduct and therefore larger R_N values (Figure 6).

For ASW-covered N_2O_4 , the R_N values for second, third, etc. pulses are larger than that of the first pulse. This is consistent with N_2O_4 being present at or near the surface due to the first pulse, with subsequent pulses displaying signatures of exposed N_2O_4 . For example, note the pulse-2 entries in Table 2. In the same vein, under low-fluence conditions, additional pulses are required to bring N_2O_4 to vacuum. Also, the fact that facile H/D exchange occurs when the upper ASW is composed of H_2O and D_2O layers indicates that water that reaches the mass spectrometer has been entrained by heated material moving through fissures.

The above observations augur for material reaching vacuum via fissures. For all practical purposes, it is impossible for material to wend its way diffusively through porous ASW without freezing. Aspects of the model are described below, starting with a phenomenon that caught our attention from the start: exceptionally long time scales for material arriving at the ionization region.

4.2. Time Scales. Temporal profiles proved to be central to establishing transport mechanisms. Their time scales often exceeded 1 ms, and this plus their lumpy character surprised us. Experiments were repeated and scrutinized over many months, varying conditions widely. We found that the main character is robust. Lumps differ from one profile to the next, but the profiles always display lumpy character, especially at long times. It is a signature of the processes whereby material enters vacuum.

As mentioned earlier, it is not feasible that H_2O molecules leave the surface at $t = 0$ and arrive $1200\ \mu\text{s}$ later at the ionization region without undergoing collisions. Were collision-free transit to commence at $t = 0$, the kinetic energy for a $1200\ \mu\text{s}$ arrival time would be a minuscule $0.33\ \text{cm}^{-1}$. Even for an arrival time of $150\ \mu\text{s}$, it would be only $21\ \text{cm}^{-1}$. Such low kinetic energies cannot be assigned to the tail of a distribution. For example, in Figure 10a, which is typical, only $\sim 4\%$ of the signal lies within $150\ \mu\text{s}$.

These observations are consistent with the majority of the water molecules that leave the film at $t = 0$ arriving at the ionization region after undergoing collisions. Delayed departure after the laser firing would require at least hundreds of microseconds. The region emitting the molecules would have to have lost thermal contact with the rest of the film, and to an incredible extent. We deem this unlikely on the basis of the heat transfer calculations described below. We also deem it unlikely that large chunks of water are liberated that eventually reach the ionization region. No cluster ions were observed, though they are readily observed using other excitation methods.⁸ The large-chunks mechanism is also inconsistent with the efficient H/D exchange observed using layered samples. We conclude that the fissures and their effluents are key to understanding the long-time signals.

4.3. Fissures. The data are consistent with porous ASW undergoing morphological change when subjected to temperature and pressure gradients. For a laser beam diameter of 0.3 mm and a film thickness of 300 nm, the diameter-to-thickness ratio is 10^3 . Because ASW must maintain its macroscopic column density, there is a propensity to develop fissures. Heated fluid is composed of N_xO_y and entrained water, and its upward thrust also promotes fissure formation. The robust nature of large fissures is supported by the second, third, etc. pulse data.

Fissures that yield signal probably involve a reasonably direct path from the N_2O_4 layer to vacuum. Material cannot follow a trajectory that twists and turns without freezing. Were an ASW density of $0.8\ \text{g cm}^{-3}$ to convert completely to crystalline ice and vertical fissures, the fissures would account for roughly 13% of the surface area. This is not achieved, as evidenced by the large number of pulses needed to deplete the N_2O_4 reservoir.

The effluent from a given fissure collides with effluents from nearby fissures (Figure 14). Regardless of angular spread, direction of main flow, or fissure shape, there is too much opening per unit area to not have collisions above the film surface, where the density of ejected material is high. It is not feasible that low-density gas travels through the fissures, as it

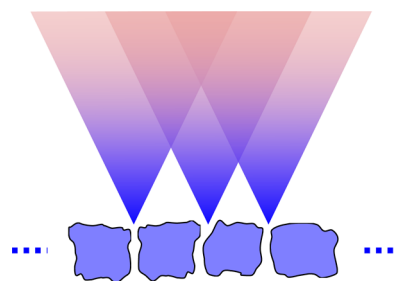


Figure 14. Cartoon illustrating how fissure effluents might interact.

would deposit on the walls. The material that makes its way to vacuum is liquid and/or high-density gas. As explained below, rapid cooling sets in near the film–vacuum interface following cessation of the 10 ns pulse. ASW in this region cannot be heated to any significant degree through diffusive heat transfer.

Collisions between effluents from different fissures will deflect species in many directions, giving rise to collisions with metal surfaces and bouncing around within the region bounded by metal surfaces. This results in a spatially inhomogeneous density in the extraction region. We propose that this is responsible for the lumpy character at long times.

The picture that emerges is that pulsed heating creates pressure and temperature gradients, resulting in fissures that connect the N_2O_4 reservoir to vacuum. Heated N_xO_y removes water from fissure walls and carries it along. The pulse duration is long enough to heat N_xO_y as it passes through fissures, maintaining a warm fluid. The radiation also photodissociates N_2O_4 that has entered the gas phase prior to the pulse's termination.

4.4. Material Transport. The high-density environment converts absorbed 266 nm radiation to heat, and temperature and pressure gradients initiate morphological change in the ASW. Column densities are maintained over large horizontal length scales, whereas fissures form on smaller scales. Many are wide enough to enable fluid to reach vacuum with the first pulse. Such fissures are expected to be robust.

Heat flow in layered films was calculated using the program COMSOL Multiphysics. The goal was to judge qualitatively how films cool following pulsed excitation, particularly near the vacuum interface. Thermal contact between layers was assumed, and phase changes and thermal desorption were neglected. Densities were held constant: 3.6, 0.8, and $2.0\ \text{g cm}^{-3}$ for MgO , ASW, and N_2O_4 , respectively.^{21,26–28} Thermal conductivities are less certain. The 100 K values chosen were 250, 1, and $1\ \text{W m}^{-1}\ \text{K}^{-1}$, respectively,^{21,22,29} on the basis of literature values and the uncertain nature of our samples, particularly following pulsed excitation. The heat capacities of ASW and N_2O_4 vary linearly with temperature above 90 K,^{30,31} so they were extrapolated to higher temperatures. A range of thermal conductivity values was explored.

Figure 15 shows representative plots of calculated surface temperature versus time for starting temperatures of 400 K for N_2O_4 and 100 K for MgO and ASW. For 2400 ML, the peak temperature is reached at 170 ns, with no temperature increase at 10 ns. For 1200 ML, the peak is at 60 ns, again with no temperature increase at 10 ns. For 600 ML, the peak is at 30 ns, with an increase of 20 K at 10 ns.

In the experiments, material that enters vacuum removes heat, and the ASW insulation layer absorbs heated N_2O_4 , thereby improving thermal conductivity to the MgO substrate. Moreover, no discernible degree of crystallinity has ever been

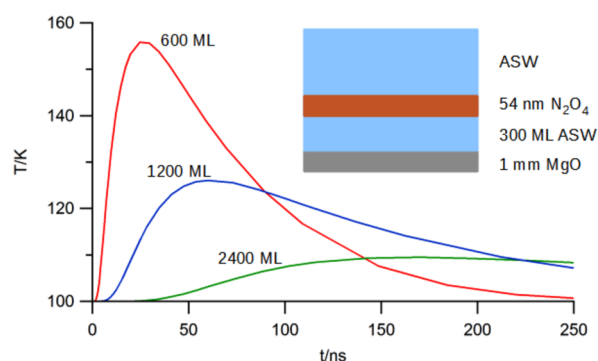


Figure 15. Film surface temperature versus time. N_2O_4 starts at 400 K; everything else starts at 100 K. At 10 ns, the 600, 1200, and 2400 nm upper ASW layers are at 120, 100, and 100 K, respectively. These calculated temperatures are upper bounds.

observed in FTIR spectra in either the insulation layer or the upper ASW following irradiation. Upon cessation of the 10 ns pulse, material in the fissures begins to cool. In light of its proximity to surrounding ASW, it quickly freezes. On this basis, we estimate that for a 2400 nm layer material passes through fissures with a minimum speed of order 10^2 m/s.

The above picture is consistent with the data. Even with 2400 ML of ASW, a large amount of N_2O_4 enters vacuum with the first pulse, which would not happen without it passing through fissures as a fluid. The first pulse deposits N_2O_4 at or near the surface. Considering Figure 11, there is striking similarity between the N_xO_y signals observed for the second pulses and those associated with exposed N_2O_4 . This correspondence persists for subsequent pulses up to the largest number used (~ 70). This supports the proposed model, in which repeated photoexcitation pumps N_2O_4 from its reservoir to the surface through robust fissures.

Another result that is consistent with the model is that when the fluence is lowered to below the threshold for material release into vacuum, it takes two or more pulses to observe N_xO_y signals. When the heated fluid lacks the thrust necessary to enter vacuum, cooling traps material and its release to vacuum awaits the next pulse. The model also reconciles the facile H/D exchange that takes place when using $\text{H}_2\text{O}/\text{D}_2\text{O}$ layers. Exchange was efficient regardless of whether the D_2O layer is above or below the H_2O layer. These data demonstrate that water is stripped from fissure walls throughout transport. It will be informative to examine exchange using pulses of ~ 20 ps duration, as this separates (temporally) photoexcitation from transport.

5. SUMMARY

An experimental approach has been developed for studying laser-initiated material transport and removal in layered films of ASW and N_2O_4 . A MgO substrate at 100 K is covered with an ASW layer to insulate heated N_2O_4 from the MgO substrate, which has high thermal conductivity. The N_2O_4 layer is covered with up to 2400 ML of ASW. Pulsed 266 nm irradiation (10 ns; 1 mJ, focused with a 50 cm lens to ~ 0.3 mm diameter) heats N_2O_4 , and we propose that material flow takes place through fissures that extend from the N_2O_4 layer to vacuum. Temporal profiles and mass spectra (at 10 μs intervals) following a single pulse provide information on timescales and transport mechanisms.

The microcosm created in these studies is challenging insofar as developing a quantitative, predictive model. Nonetheless, qualitative understanding has been achieved, with trends and phenomena in line with predictions. A quantitative model will require a combination of laboratory and computational work. The main features of the current model are summarized below.

Laser-initiated heating of the N_2O_4 layer results in fissures that connect the heated layer to vacuum. The pressure of the heated fluid provides thrust that launches material toward the surface. Fissures allow transport of heated material to vacuum without freezing on the walls. Many of the fissures are robust, surviving many pulses. It is possible to halt the flow of heated fluid prior to it entering vacuum by reducing the fluence. Subsequent irradiation causes fluid to enter vacuum, and this fracking-like pumping continues with consecutive laser pulses. Efficient H/D scrambling using alternating H_2O and D_2O layers demonstrate that water is removed from fissure walls and entrained in fluid flow. There is interplay between the fluid freezing onto fissure walls versus removal of water from the fissure walls by the heated fluid.

Heated material reaches vacuum with a single pulse. As the thickness of the upper ASW layer is increased, the fractional amount of water that enters vacuum increases, presumably because warm fluid passes over more fissure area. The N_xO_y -rich fluid that moves through the fissures continues to be heated as long as the pulse is on. Figure 15 indicates that cooling is efficient enough that fluid in a fissure freezes shortly after termination of the pulse. This can be used to obtain a rough lower bound of the speed with which fluid passes through fissures toward vacuum.

For a 1000 nm thick ASW layer, material that travels through the fissures does so at 100 m/s or faster. Had the speed been lower, material that commenced travel at the N_2O_4 layer with the onset of the laser pulse would freeze before it reached the sample surface. In other words, material moving toward the surface would freeze on the fissure wall. With thinner samples, it follows that a significant amount of effluent enters the gas phase within the duration of the laser pulse. This is consistent with our observation of early N_xO_y arrival times at the ionization region as well as the presence of NO_2 , presumably due to N_2O_4 266 nm photodissociation.

Fissure density is high enough to enable collisions between effluents from different fissures. This rationalizes long arrival times at the ionization region, e.g., >1 ms, and the lumpy appearance of the temporal profiles. We propose that ejected material undergoes collisions with other molecules and metal surfaces and takes a circuitous path before reaching the ionization region.

Similarities between the phenomena observed in this study and those on Enceladus are noteworthy despite the enormous scale differences. Enceladus has a subsurface ocean of liquid water below a solid water mantle 30–40 km thick. Nevertheless, stresses due to gravitational interactions cause fissures in the ice that expand and contract, releasing water that contains small molecules. This fluid is transported through fissures, and jets are observed. Though beyond the scope of this paper, such similarities are intriguing.

In closing, it would be useful to characterize material transport through fissures more quantitatively, i.e., by preparing fissures whose properties are known and controllable. We have obtained preliminary results along these lines using a sparse density of gold nanospheres on MgO. Such particles serve as

templates for creating channels in ASW through deposition and pulsed heating.

■ APPENDIX

An expression is derived for the ratio of the NO₂ and N₂O₄ concentrations that reach the ionization region of the mass spectrometer. It is in terms of ionization cross-sections, parent ion fragmentation patterns, and relative ion signals. For example, use is made of measured quantities such as NO⁺/NO₂⁺, where NO⁺ and NO₂⁺ denote the areas of the respective ion signals. It is assumed that the microchannel plate detector has equal sensitivity for each ion. To begin, expressions for the amounts (concentrations) of NO₂⁺, NO⁺, and O⁺ are written

$$\text{NO}_2^+ = \sigma_{\text{N}_2\text{O}_4}^{\text{ion}} F_{\text{N}_2\text{O}_4}^{\text{NO}_2^+} \text{N}_2\text{O}_4 + \sigma_{\text{NO}_2}^{\text{ion}} F_{\text{NO}_2}^{\text{NO}_2^+} \text{NO}_2 \quad (\text{A.1})$$

$$\text{NO}^+ = \sigma_{\text{N}_2\text{O}_4}^{\text{ion}} F_{\text{N}_2\text{O}_4}^{\text{NO}^+} \text{N}_2\text{O}_4 + \sigma_{\text{NO}_2}^{\text{ion}} F_{\text{NO}_2}^{\text{NO}^+} \text{NO}_2 + \sigma_{\text{NO}}^{\text{ion}} F_{\text{NO}}^{\text{NO}^+} \text{NO} \quad (\text{A.2})$$

$$\begin{aligned} \text{O}^+ &= \sigma_{\text{N}_2\text{O}_4}^{\text{ion}} F_{\text{N}_2\text{O}_4}^{\text{O}^+} \text{N}_2\text{O}_4 + \sigma_{\text{NO}_2}^{\text{ion}} F_{\text{NO}_2}^{\text{O}^+} \text{NO}_2 + \sigma_{\text{H}_2\text{O}}^{\text{ion}} F_{\text{H}_2\text{O}}^{\text{O}^+} \\ &+ \sigma_{\text{NO}}^{\text{ion}} F_{\text{NO}}^{\text{O}^+} \text{NO} + \sigma_{\text{O}}^{\text{ion}} \text{O} \end{aligned} \quad (\text{A.3})$$

where σ_X^{ion} is the 70 eV ionization cross section for the neutral species X, and $F_X^{Y^+}$ is the fraction of daughter ion Y⁺ that arises from fragmentation of the parent ion X⁺.

The use of equal signs rather than proportionality constants in eqs A.1–A.3 is in anticipation of the fact that these constants would cancel were they carried along. The relatively small amount of O₂⁺ that appears in spectra shall be ignored. Likewise, it is assumed that the NO and O concentrations are negligible. This is a safe assumption for long arrival times at the ionization region, less so for short arrival times.

To proceed, the last term in eq A.2 and the last two terms in eq A.3 are dropped, in which case eq A.3 is decoupled from eqs A.1 and A.2. Considering eq A.2, NO⁺ = (NO⁺/NO₂⁺) NO₂⁺ is introduced. Combining eqs A.1 and A.2 then yields

$$\begin{aligned} (\text{NO}^+/\text{NO}_2^+) (\sigma_{\text{N}_2\text{O}_4}^{\text{ion}} F_{\text{N}_2\text{O}_4}^{\text{NO}_2^+} \text{N}_2\text{O}_4 + \sigma_{\text{NO}_2}^{\text{ion}} F_{\text{NO}_2}^{\text{NO}_2^+} \text{NO}_2) \\ = \sigma_{\text{N}_2\text{O}_4}^{\text{ion}} F_{\text{N}_2\text{O}_4}^{\text{NO}^+} \text{N}_2\text{O}_4 + \sigma_{\text{NO}_2}^{\text{ion}} F_{\text{NO}_2}^{\text{NO}^+} \text{NO}_2. \end{aligned} \quad (\text{A.4})$$

Separating this into separate terms for NO₂ and N₂O₄ gives

$$\begin{aligned} \text{NO}_2 \sigma_{\text{NO}_2}^{\text{ion}} ((\text{NO}^+/\text{NO}_2^+) F_{\text{NO}_2}^{\text{NO}_2^+} - F_{\text{NO}_2}^{\text{NO}^+}) \\ = \text{N}_2\text{O}_4 \sigma_{\text{N}_2\text{O}_4}^{\text{ion}} (F_{\text{N}_2\text{O}_4}^{\text{NO}^+} - (\text{NO}^+/\text{NO}_2^+) F_{\text{N}_2\text{O}_4}^{\text{NO}_2^+}) \end{aligned} \quad (\text{A.5})$$

Further rearrangement yields the desired ratio

$$\frac{\text{NO}_2}{\text{N}_2\text{O}_4} = 2.08 \frac{(\text{NO}^+/\text{NO}_2^+) F_{\text{N}_2\text{O}_4}^{\text{NO}_2^+} - F_{\text{N}_2\text{O}_4}^{\text{NO}^+}}{F_{\text{NO}_2}^{\text{NO}^+} - (\text{NO}^+/\text{NO}_2^+) F_{\text{NO}_2}^{\text{NO}_2^+}} \quad (\text{A.6})$$

where $\sigma_{\text{N}_2\text{O}_4}^{\text{ion}}/\sigma_{\text{NO}_2}^{\text{ion}} = 2.08$ has been used (Table 1). Equation A.6 can be used to obtain relative NO₂ and N₂O₄ concentrations when NO and O are in low enough concentration to justify ignoring them.

■ ASSOCIATED CONTENT

Supporting Information

The file contains spectra that corroborate the behavior shown in Figure 10, which shows irregular temporal profiles that are characteristic of the mechanism whereby material enters the

vacuum, through further illustration of the effect. The Supporting Information is available free of charge on the ACS Publications website at DOI: 10.1021/jp510861u.

■ AUTHOR INFORMATION

Corresponding Authors

*E-mail: reisler@usc.edu. Tel.: (213) 740-7071.

*E-mail: wittig@usc.edu. Tel.: (213) 740-7368.

Author Contributions

†The first three authors (J.S., S.M., and C.L.) contributed equally. The order of names was chosen randomly.

Notes

The authors declare no competing financial interest.

■ ACKNOWLEDGMENTS

Technical development of methodology was supported by the U.S. Department of Energy, Office of Basic Energy Sciences under Grant DE-SC0003976. Some graduate student support was provided through endowed chairs (H.R. and C.W.).

■ REFERENCES

- (1) Angell, C. A. Amorphous Water. *Annu. Rev. Phys. Chem.* **2004**, *55*, 559–583.
- (2) Hama, T.; Watanabe, N. Surface Processes on Interstellar Amorphous Solid Water: Adsorption, Diffusion, Tunneling Reactions, and Nuclear-Spin Conversion. *Chem. Rev. (Washington, DC, U.S.)* **2013**, *113*, 8783–8839.
- (3) Porco, C. C. Cassini Observes the Active South Pole of Enceladus. *Science* **2006**, *311*, 1393–1401.
- (4) Hansen, C. J. Enceladus' Water Vapor Plume. *Science* **2006**, *311*, 1422–1425.
- (5) Porco, C.; DiNino, D.; Nimmo, F. How the Geysers, Tidal Stresses, and Thermal Emission Across the South Polar Terrain of Enceladus are Related. *Astron. J.* **2014**, *148*, 45.
- (6) May, R. A.; Smith, R. S.; Kay, B. D. The Release of Trapped Gases from Amorphous Solid Water Films. I. "Top-Down" Crystallization-Induced Crack Propagation Probed Using the Molecular Volcano. *J. Chem. Phys.* **2013**, *138*, 104501.
- (7) May, R. A.; Scott Smith, R.; Kay, B. D. The Release of Trapped Gases from Amorphous Solid Water Films. II. "Bottom-Up" Induced Desorption Pathways. *J. Chem. Phys.* **2013**, *138*, 104502.
- (8) Rebolledo-Mayoral, O.; Stomberg, J.; McKean, S.; Reisler, H.; Wittig, C. Amorphous Solid Water (ASW): Pulsed Laser Ablation of ASW/CO₂ Thin Films. *J. Phys. Chem. C* **2012**, *116*, 563–569.
- (9) Dohnálek, Z.; Kimmel, G. A.; Ayotte, P.; Smith, R. S.; Kay, B. D. The Deposition Angle-Dependent Density of Amorphous Solid Water Films. *J. Chem. Phys.* **2003**, *118*, 364–372.
- (10) Johari, G. P.; Hallbrucker, A.; Mayer, E. The Glass–Liquid Transition of Hyperquenched Water. *Nature* **1987**, *330*, 552–553.
- (11) May, R. A.; Smith, R. S.; Kay, B. D. The Molecular Volcano Revisited: Determination of Crack Propagation and Distribution During the Crystallization of Nanoscale Amorphous Solid Water Films. *J. Phys. Chem. Lett.* **2012**, *3*, 327–331.
- (12) Hawkins, S.; Kumi, G.; Malyk, S.; Reisler, H.; Wittig, C. Temperature Programmed Desorption and Infrared Spectroscopic Studies of Thin Water Films on MgO(100). *Chem. Phys. Lett.* **2005**, *404*, 19–24.
- (13) Kumi, G.; Malyk, S.; Hawkins, S.; Reisler, H.; Wittig, C. Amorphous Solid Water Films: Transport and Guest–Host Interactions with CO₂ and N₂O Dopants. *J. Phys. Chem. A* **2006**, *110*, 2097–2105.
- (14) Malyk, S.; Kumi, G.; Reisler, H.; Wittig, C. Trapping and Release of CO₂ Guest Molecules by Amorphous Ice. *J. Phys. Chem. A* **2007**, *111*, 13365–13370.

- (15) Korolik, M.; Suchan, M. M.; Johnson, M. J.; Arnold, D. W.; Reisler, H.; Wittig, C. Survival of $\text{HCl}(v=2)$ in Trapping-Desorption From $\text{MgO}(100)$. *Chem. Phys. Lett.* **2000**, 326, 11–21.
- (16) Linstrom, P. J.; Mallard, W. G. *NIST Chemistry WebBook, NIST Standard Reference Database Number 69*. National Institute of Standards and Technology: Gaithersburg, MD; <http://webbook.nist.gov>, (Accessed October 17, 2014).
- (17) Dixon-Warren, S. J.; Jackson, R. C.; Polanyi, J. C.; Rieley, H.; Shapter, J. G.; Weiss, H. Photodissociation of Nitrogen Dioxide Adsorbed on Lithium Fluoride (001). *J. Phys. Chem.* **1992**, 96, 10983–10994.
- (18) Hisatsune, I. C. Thermodynamic Properties of Some Oxides of Nitrogen 1. *J. Phys. Chem.* **1961**, 65, 2249–2253.
- (19) Russ, F. The Vapor Pressure Curve of Solid Nitrogen Tetroxide. *Z. Phys. Chem.* **1914**, 82, 217–222.
- (20) Kim, Y. K.; Rudd, M. E. Binary-Encounter-Dipole Model for Electron-Impact Ionization. *Phys. Rev. A: At., Mol., Opt. Phys.* **1994**, 50, 3954–3966.
- (21) Slack, G. A. Thermal Conductivity of MgO , Al_2O_3 , MgAl_2O_4 , and Fe_3O_4 Crystals from 3 to 300 K. *Phys. Rev.* **1962**, 126, 427–441.
- (22) Andersson, O.; Suga, H. Thermal Conductivity of Amorphous Ices. *Phys. Rev. B: Condens. Matter Mater. Phys.* **2002**, 65, 140201.
- (23) Kim, S.-K.; Kang, H. Efficient Conversion of Nitrogen Dioxide Into Nitrous Acid on Ice Surfaces. *J. Phys. Chem. Lett.* **2010**, 1, 3085–3089.
- (24) Lignell, H.; Varner, M. E.; Finlayson-Pitts, B. J.; Benny Gerber, R. Isomerization and Ionization of N_2O_4 on Model Ice and Silica Surfaces. *Chem. Phys.* **2012**, 405, 52–59.
- (25) Park, S.-C.; Jung, K.-H.; Kang, H. H/D Isotopic Exchange Between Water Molecules at Ice Surfaces. *J. Chem. Phys.* **2004**, 121, 2765–2774.
- (26) Westley, M. S.; Baratta, G. A.; Baragiola, R. A. Density and Index of Refraction of Water Ice Films Vapor Deposited at Low Temperatures. *J. Chem. Phys.* **1998**, 108, 3321–3326.
- (27) Stevenson, K. P.; Kimmel, G. A.; Dohnálek, Z.; Smith, R. S.; Kay, B. D. Controlling the Morphology of Amorphous Solid Water. *Science* **1999**, 283, 1505–1507.
- (28) Kvick, Å.; McMullan, R. K.; Newton, M. D. The Structure of Dinitrogen Tetroxide N_2O_4 : Neutron Diffraction Study at 100, 60, and 20 K and Ab Initio Theoretical Calculations. *J. Chem. Phys.* **1982**, 76, 3754–3761.
- (29) Sumarokov, V. V.; Stachowiak, P.; Mucha, J.; Jeżowski, A. Low-Temperature Thermal Conductivity of Cryocrystals Formed by Linear Three-Atom Molecules. *Phys. Rev. B: Condens. Matter Mater. Phys.* **2006**, 74, 224302.
- (30) Handa, Y. P.; Klug, D. D. Heat Capacity and Glass Transition Behavior of Amorphous Ice. *J. Phys. Chem.* **1988**, 92, 3323–3325.
- (31) Giauque, W. F.; Kemp, J. D. The Entropies of Nitrogen Tetroxide and Nitrogen Dioxide. The Heat Capacity from 15°K to the Boiling Point. The Heat of Vaporization and Vapor Pressure. The Equilibria $\text{N}_2\text{O}_4=2\text{NO}_2=2\text{NO}+\text{O}_2$. *J. Chem. Phys.* **1938**, 6, 40–51.